2005

Microwave backscatter modeling of erg surfaces in the Sahara Desert

Haroon Stephen
University of Nevada, Las Vegas, haroon.stephen@unlv.edu

David G. Long
Brigham Young University - Utah, long@ee.byu.edu

Repository Citation

Stephen, H., Long, D. G. (2005). Microwave backscatter modeling of erg surfaces in the Sahara Desert. *IEEE Transactions on Geoscience and Remote Sensing, 43*(2), 238-247. Institute of Electrical and Electronics Engineers.
http://dx.doi.org/10.1109/TGRS.2004.840646

Microwave Backscatter Modeling of Erg Surfaces in the Sahara Desert

Haroon Stephen, *Student Member, IEEE,* and David G. Long, *Senior Member, IEEE*

***Abstract*—The Sahara desert includes large expanses of sand dunes called ergs. These dunes are formed and constantly reshaped by prevailing winds. Previous study shows that Saharan ergs exhibit significant radar backscatter (σ°) modulation with azimuth angle (ϕ). We use σ° measurements observed at various incidence angles and ϕ from the NASA Scatterometer (NSCAT), the SeaWinds scatterometer, the ERS scatterometer (ESCAT), and the Tropical Rainfall Measuring Mission's Precipitation Radar to model the σ° response from sand dunes. Observations reveal a characteristic relationship between the backscatter modulation and the dune type, i.e., the number and orientation of the dune slopes. Sand dunes are modeled as a composite of tilted rough facets, which are characterized by a probability distribution of tilt with a mean value, and small ripples on the facet surface. The small ripples are modeled as cosinusoidal surface waves that contribute to the return signal at Bragg angles only. Longitudinal and transverse dunes are modeled with rough facets having Gaussian tilt distributions. The model results in a σ° response similar to NSCAT and ESCAT observations over areas of known dune types in the Sahara. The response is high at look angles equal to the mean tilts of the rough facets and is lower elsewhere. This analysis provides a unique insight into scattering by large-scale sand bedforms.**

***Index Terms*—Backscatter, erg, ERS Scatterometer (ESCAT), NASA Scatterometer (NSCAT), sand dune, sand sheet, SeaWinds Scatterometer (QSCAT), Tropical Rainfall Measuring Mission Precipitation Radar (TRMM-PR).**

I. Introduction

DESERTS comprise more than 20% of the world's land surface [1]. Deserts consist of diverse terrains primarily classified as rocky mountains, small- and large-scale-gravel zones, and vast sand-seas called *hamadas*, *regs*, and *ergs*, respectively. Ergs constitute more than a quarter of the global desert surface [2]. The Sahara desert is the largest desert and one of the most inhomogeneous regions on the earth [3]. The ergs of the Sahara consist of large sand-dune fields that are variable due to the wind action. Aeolian processes such as wind erosion and sediment transport continue to reshape the dune fields, which in turn govern the near-surface wind patterns, thus resulting in diverse and dynamic bedforms [4]. Aeolian bedform research is relatively recent. The first detailed analysis of erg geomorphology is presented in [5]. A detailed history of aeolian bedform research is presented in [1] and [2].

Satellite microwave earth remote sensing has proven to be a very useful tool for studying various earth phenomena. Scatterometers measure radar backscatter (σ°) of the surface at various incidence (θ) and azimuth (ϕ) angles. These measurements are used operationally to map surface wind fields over the ocean [6]. Land and ice σ° measurements have been used to study vegetation dynamics and ice characteristics over extended regions like the Amazon rain forest and Antarctic ice sheets [7]–[9].

Radar backscatter depends upon the geometrical and dielectric properties of the surface and varies with the look geometry. We use $\sigma^\circ(\theta, \phi)$ measurements, as function of θ and ϕ, to study the sand surface geomorphology. The $\sigma^\circ(\theta, \phi)$ measurements over ergs from the Ku-band NASA Scatterometer (NSCAT) [6], SeaWinds Scatterometer (QSCAT) [10], Tropical Rainfall Measuring Mission's Precipitation Radar (TRMM-PR) [11], and C-band ERS Scatterometer (ESCAT) [12], are used to study the surface characteristics. The key characteristics of sensors used are summarized in Table I.

A simple composite model for radar backscatter from sand dunes consisting of facets and small surface ripples is proposed. The facet model relates the surface $\sigma^\circ(\theta, \phi)$ response to the weighted sum of responses from dominant facets on the surface. Scattering from small ripples is modeled as Bragg scattering where the ripples are modeled as cosinusoidal surface waves. The amount of area covered by different facets is used to identify the type of dunes.

In this paper, we review the surface roughness hierarchy of ergs in Section II, including classification of dune shapes based upon the prevailing wind regimes and sand characteristics. In Section III, we present two simple models to relate the scatterometer backscatter to surface orientation probability distributions termed as tilt distribution and surface ripple distribution. Section IV shows the results of the forward projection of the proposed model over simulated surfaces. The results are summarized in Section V.

II. Erg Morphology

Erg bedform morphology depends upon the grain size distribution of the inherent material. Sand is generally defined as particles 0.0625–2.0 mm in diameter [13]. The proportion of different particles and mixing of clay particles play an important role in the aeolian transport. Ergs consist of a hierarchy of aeolian bedforms consisting of three components called *ripples*, *dunes*, and *draas*. Some erg areas also exist as sand sheets with no dominant dunes. Some sand sheets have small-scale ripples due to wind action. Under the action of wind, sand grain entrainment and deposition result in surface undulations in the form of surface ripples. Surface ripple patterns are repetitive in the downwind direction and can have wavelengths of 1–25 cm and amplitudes of 0.2–5 cm. The ripples have a quick response to

Manuscript received June 1, 2004; revised October 20, 2004.

The authors are with the Center for Earth Remote Sensing, Brigham Young University, Provo, UT 84602 USA (e-mail: hs92@et.byu.edu; long@ee.byu.edu).

Digital Object Identifier 10.1109/TGRS.2004.840646

TABLE I
LIST OF SENSORS USED AND KEY SPECIFICATIONS

Sensor	Platform	Years	Frequency (GHz)	Polarization	Resolution (km)	Incidence Angle (deg)
ESCAT	ERS-1/2	1991-2000	5.3	V	50	20°-70°
NSCAT	ADEOS	1996-1997	14.0	H V	50	17°-62°
QSCAT	SeaWinds	1999-	13.4	H V	25	46° & 54°
TRMM-PR	TRMM	1997-	13.8	H	4.2	0°-17°

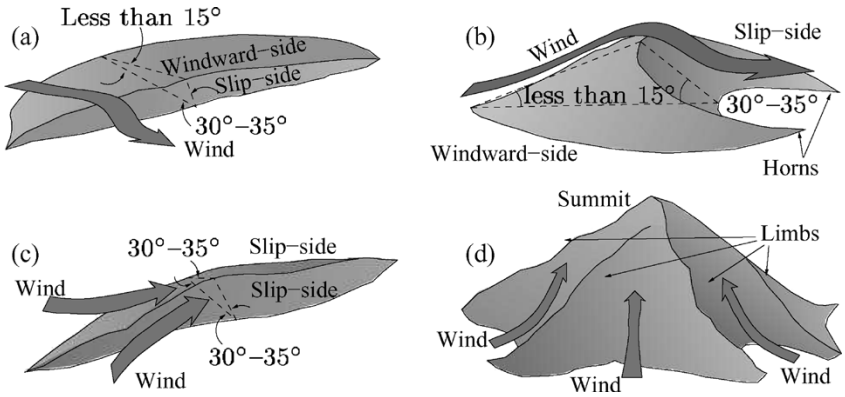

Fig. 1. Diagram illustrating the shapes of (a) transverse, (b) barchan, (c) longitudinal, and (d) star dunes.

local wind variations that can indicate short-term changes in the wind direction.

Dunes are formed by sand deposition in the lee of a rock or a bush over extended periods of time. They occur in various forms depending upon the prevailing wind regimes and available sand material. Dunes have 3–600 m wavelength and 0.1–100 m amplitude. Most dunes include at least one slip-side that is formed by the sand sliding from the dune summit and has a slope equal to the angle of repose of sand (30° to 35°). There may be other sides that have shallower slopes than the slip-side. The number of sides and their slopes are used to characterize the type of the dune [4].

Erg bedform hierarchies depend upon both sand and wind characteristics, including the wind speed and direction and their annual variabilities. The annual distribution of the wind direction may be characterized as narrow or wide unimodal, acute or obtuse bimodal, or complex (multimodal) based on its directional variability over time. Narrow unimodal, wide unimodal, and acute bimodal wind direction distributions result in *transverse* dunes where the dune axis is perpendicular to the average wind direction as shown in Fig. 1(a). The downwind side is a slip-side whereas the upwind side, called the windward-side, has a slope of 10° to 15°. For a limited supply of sand mass, similar wind regimes result in crescent-shaped dunes (Barchans) shown in Fig. 1(b). Obtuse bimodal wind direction distributions form *longitudinal* dunes [Fig. 1(c)] that have axes almost parallel to the average wind direction. Such dunes are characterized by two slip-sides, one on each side of the central ridge. Both transverse and longitudinal dunes can extend to a few kilometers and occur in the form of dune fields with interdune flat areas. Complex wind direction distributions result in complex dune formations. The most common formation is called a *star* or *pyramidal* dune [Fig. 1(d)], which has multiple limbs extending from a summit. Complex winds can also result in the complex forms consisting of mixtures of the simpler dune forms [13].

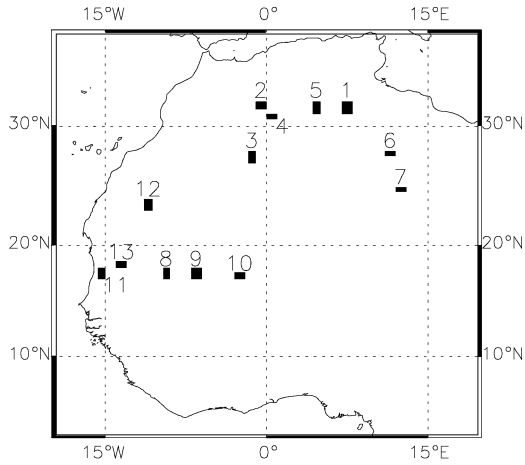

Fig. 2. Map of the study area showing selected sites. Sites 2, 5, and 9 are sand sheets. Sites 6, 7, 8, and 13 are transverse dunes. Sites 10 and 11 are longitudinal dunes. Sites 1, 3, 4, and 12 are complex dunes.

Thirteen sites in various ergs of the Sahara desert that include transverse, longitudinal, and complex dune types are selected to study the σ° response from different dune shapes. A map showing the selected sites is presented in Fig. 2. The site information is extracted from [13].

III. SURFACE BACKSCATTER MODEL

The total backscattering coefficient $\sigma^\circ(\theta, \phi)$ from the sand as a function of incidence and azimuth angle is modeled as

$$\sigma^\circ(\theta,\phi) = \sigma^\circ_{\text{surf}}(\theta,\phi) + \sigma^\circ_{\text{vol}}(\theta) \tag{1}$$

where $\sigma^\circ_{\text{surf}}(\theta, \phi)$ is surface scattering in the θ, ϕ direction, and $\sigma^\circ_{\text{vol}}(\theta)$ is volume scattering as a function of incidence angle. The model is shown pictorially in Fig. 3. The volume scattering component results from incident electromagnetic waves

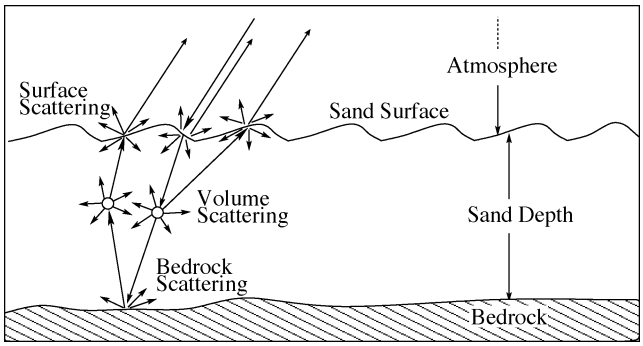

Fig. 3. Diagram showing a simple sand surface with surface and volume scattering components.

that have penetrated into the subsurface. Sand material generally has a very low dielectric constant, and this allows the electromagnetic waves to penetrate as deep as the parent bedrock, depending on the moisture content of the sand. Scattering from the subsurface is primarily caused by the sand particles, which are assumed to be homogeneous and result in isotropic backscattering. A simple volume scattering model presented in [14] is used to estimate the volume backscatter contribution. We use nominal values for the model parameters, e.g., the number density of sand particles of 4000 particles/cm^3, a cross section per scatterer of -10^{-7} dB/particle, and an attenuation coefficient of 0.05 dB/cm. With these values, the sand volume scattering contribution is estimated to be small (-5 dB or less) relative to the total scattering so that we can ignore the volume scattering component and model the return backscatter as the contribution from only the sand surface.

Surface scattering is predominantly due to the geometric characteristics of the surface. The erg surface profile has two main spatial frequency components, corresponding to the two predominant land features. The low spatial frequency (wavenumber) components are due to large-scale dunes, whereas the high-wavenumber components are due to small ripples on the surface of the dunes. Following the two scale approach used for ocean waves [15], the surface scattering coefficient can be decomposed into separate surface scattering components from dunes and ripples, i.e.,

$$\sigma^{\circ}_{\text{surf}}(\theta,\phi) = \sigma^{\circ}_{\text{dunes}}(\theta,\phi) + \sigma^{\circ}_{\text{ripples}}(\theta,\phi) \tag{2}$$

where $\sigma^{\circ}_{\text{dunes}}(\theta,\phi)$ is the surface scattering from large-scale dunes, and $\sigma^{\circ}_{\text{ripples}}(\theta,\phi)$ is the surface scattering from small-scale ripples on the dunes, which is affected by local tilt. $\sigma^{\circ}_{\text{dunes}}(\theta,\phi)$ and $\sigma^{\circ}_{\text{ripples}}(\theta,\phi)$ are the contributions from low- and high-frequency vertical variations of the surface, respectively. Observations suggest that $\sigma^{\circ}_{\text{ripples}}(\theta,\phi)$ is dominated by Bragg scattering that occurs at discrete θ and ϕ. The look directions at which Bragg scattering occurs are dependent on the spectrum of the small-scale ripples.

We model the sand surface as a composite of tilted rough facets with cosinusoidal ripples (corresponding to the small ripples). Fig. 4 depicts one such tilted rough facet. $\hat{\mathbf{n}}$ denotes the rough facet unit normal vector that is oriented in the (θ_s,ϕ_s) direction in spherical coordinates. The rough facet is characterized by a probability distribution of tilt $P(\theta_s,\phi_s)$ with a mean

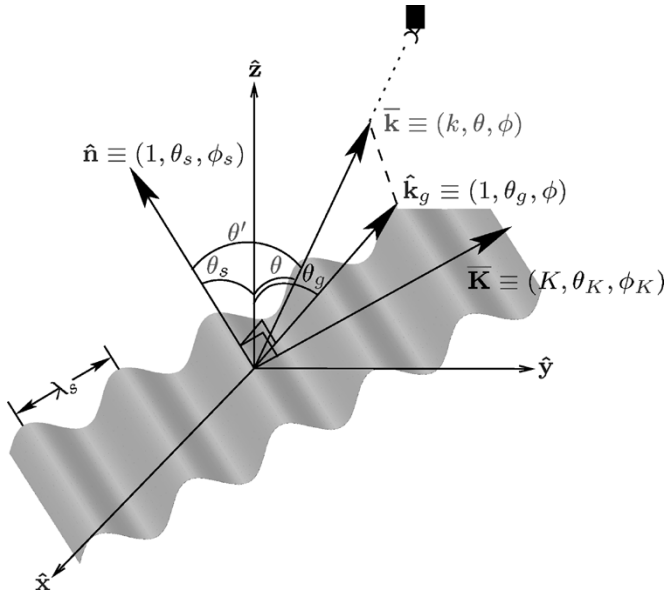

Fig. 4. Model of tilted rough facet with cosinusoidal surface ripples.

(θ_n,ϕ_n). $\overline{\mathbf{k}}$ denotes the incident wave vector with a wavelength λ and wavenumber $k = 2\pi/\lambda$. It is represented by $(k,\ \theta,\ \phi)$ in spherical coordinates where θ and ϕ are the incidence and azimuth angles of the incident wave. $\hat{\mathbf{k}}_g$ is a unit vector in the direction of the projection of $\overline{\mathbf{k}}$ on the facet. The incidence angle of $\hat{\mathbf{k}}_g$ is called grazing angle (θ_g), which depends on facet tilt θ_s and sensor azimuth angle ϕ. For $\theta > \theta_g$, the facet is not illuminated. $\overline{\mathbf{K}}$ represents the wave vector of the surface cosinusoidal ripples with wavelength λ_s and wavenumber $K = 2\pi/\lambda_s$. $(K,\ \theta_K,\ \phi_K)$ are the spherical coordinates of $\overline{\mathbf{K}}$. $\overline{\mathbf{K}}$ is always perpendicular to $\hat{\mathbf{n}}$. Vectors $\hat{\mathbf{n}}$, $\overline{\mathbf{k}}$, and $\overline{\mathbf{K}}$ define the sensor-surface geometry. The transformation to the local or natural coordinate system of the tilted facet gives us the local incidence (θ') and azimuth (ϕ') angles of the sensor. The derivation of θ', ϕ', and θ_g is given in the Appendix. Models for both large- and small-scale surface scattering are described in Sections III-A and III-B.

A. Rough Facet Model

In order to model the backscatter from large-scale erg surface features (i.e., dunes), we adopt the general scattering model presented in [16]. The average copolar scattering coefficient is expressed as a function of θ and ϕ given by

$$\sigma^{\circ}_{pp}(\theta,\phi) = \int_{-\infty}^{\infty}\int_{-\cot\theta}^{\infty} \sigma_{pp}(\theta',\phi) P_{\theta}(Zx', Zy') dZx dZy \tag{3}$$

where $\sigma_{pp}(\theta',\phi)$ is the generic response from the target surface as a function of azimuth angle ϕ and local incidence angle θ'. Zx and Zy are surface slopes in global x and y axis direction, respectively. The primed variables are in the local coordinate system defined by x' and z' axis in the wind flow and sensor direction, respectively. $P_{\theta}(Zx', Zy')$ is the joint probability function of the surface slope in the x' direction (Zx') and y' direction (Zy'). The joint probability distribution is modeled as a function of incidence angle. This model is also described in [17] and [18]. A similar equation has been used in [19] for

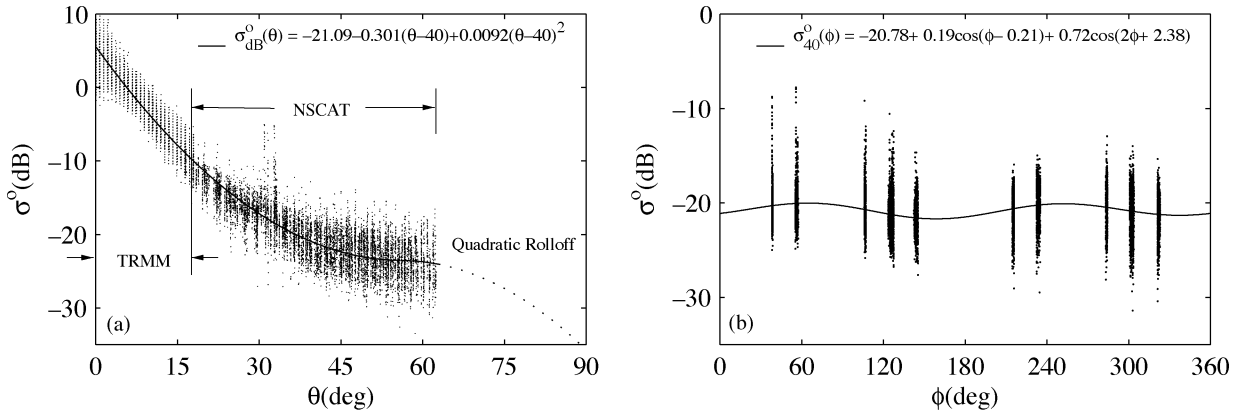

Fig. 5. (a) σ° incidence angle response at Ku-band from combined TRMM and NSCAT data, which is assumed to be the flat surface response of sand that does not vary with ϕ. A quadratic rolloff close to the grazing angles is assumed, given by $\sigma^\circ_{\rm dB} = -56.51 + 1.177\theta - 0.0105\theta^2$. (b) σ°_{40} versus ϕ with second-order harmonic fit where σ°_{40} is incidence angle corrected $\sigma^\circ_{\rm dB}$ normalized to 40°, i.e., $\sigma^\circ_{40} = \sigma^\circ_{\rm dB} + 0.301(\theta - 40^\circ) - 0.0092(\theta - 40^\circ)^2$.

a two-scale model of polarimetric emissivity. We modify this model to use the probability density function of the surface tilt angles. The backscatter from a single rough facet ($\sigma^\circ_{\rm facet}$) is modeled as

$$\sigma^\circ_{\rm facet}(\theta,\phi) = \int_0^{2\pi}\int_0^{\frac{\pi}{2}} P(\theta_s,\phi_s)\sigma_s(\theta',\phi')u(\theta_g-\theta)d\theta_s d\phi_s \quad (4)$$

where the integration is over all possible tilts in the upper hemisphere. $P(\theta_s,\phi_s)$ is the tilt distribution of the facet, and $\sigma_s(\theta',\phi')$ is the flat surface response of the sand material. θ' and ϕ' are local incidence and azimuth angles for each facet, respectively. θ_g is the facet grazing angle, and $u(\theta_g-\theta)$ is a unit step function that results in zero response when $\theta > \theta_g$.

The sand dune field is modeled as a composite of tilted rough facets. The $\sigma^\circ_{\rm dunes}(\theta,\phi)$ component of the scatterometer measurement is the sum of the returns from all the rough facets in the footprint. It is given by

$$\sigma^\circ_{\rm dunes}(\theta,\phi) = \sum_n F_n \int_0^{2\pi}\int_0^{\frac{\pi}{2}} P_n(\theta_s,\phi_s)\sigma_s(\theta',\phi') \times u(\theta_g-\theta)d\theta_s d\phi_s \quad (5)$$

where the summation is over all facets in the footprint, and F_n is the fraction of the footprint area covered by the nth rough facet. $P_n(\theta_s,\phi_s)$ is the tilt distribution of the nth rough facet. The model states that the returned power from the dune field, when an electromagnetic wave is incident from the θ and ϕ direction, is the sum of the contributions from all the surface slopes oriented to contribute to the return signal within the beam-illuminated area. The unit step function $u(\theta_g-\theta)$ assures zero return when a tilted facet is not illuminated.

We use NSCAT V-pol and TRMM-PR σ° measurements to estimate the flat surface Ku-band $\sigma_s(\theta',\phi')$ response of the surface. For a flat surface, the sensor incidence angle and local incidence angle have the same value, i.e., $\theta' = \theta$. Moreover, the response is independent of ϕ and can be written as $\sigma^\circ(\theta',\phi') = \sigma^\circ(\theta)$. NSCAT V-pol σ° observations are made over a 17° to 62° incidence angle range at ten azimuth angles, whereas TRMM σ° are at near-nadir 0° to 17° incidence angles and have very narrow azimuth angle range. Fig. 5(a) shows $\sigma^\circ(\theta')$ for NSCAT V-pol and TRMM-PR measurements over location 9 (see Fig. 2). The quadratic fit through the data is used to represent the flat surface response with no dependence on ϕ'. Lacking σ° measurements for $\theta' > 62^\circ$, a quadratic rolloff is assumed at grazing angles ($\theta' > 62^\circ$). Fig. 5(b) shows the azimuth angle response of σ° that has been corrected for incidence angle dependence.

In general, it is difficult to determine the probability distribution of the surface angles. However, by modeling sand dunes as composed of a finite number of rough facets, an estimate of the probability distribution can be made. For example, a transverse dune with a slip- and a windward-side can be modeled as two rough facets tilted at (30° to 35°, ϕ_n) and (10° to 15°, $\phi_n + 180^\circ$) mean tilt, respectively. A third facet at (0°, 0°) accounts for interdune flat area in dune fields.

Lacking a better model, we assume the surface tilt distribution to be Gaussian. If $\boldsymbol{\alpha} = [\theta_s,\phi_s]$ represents a vector whose elements are the tilt angles of the facet, then a two-dimensional Gaussian distribution for the surface tilt is given by

$$P(\theta_s,\phi_s) = P_\alpha(\alpha) = \frac{1}{2\pi\sqrt{|R_\alpha|}} e^{-\frac{1}{2}(\alpha-\mu_\alpha)R_\alpha^{-1}(\alpha-\mu_\alpha)^T} \quad (6)$$

$$\mu_\alpha = [\theta_n,\phi_n] \quad (7)$$

$$R_\alpha = \begin{bmatrix} \varsigma_\theta^2 & \varsigma_{\theta\phi} \\ \varsigma_{\phi\theta} & \varsigma_\phi^2 \end{bmatrix} \quad (8)$$

where θ_n and ϕ_n are the mean values of θ_s and ϕ_s, and ς_θ and ς_ϕ are their standard deviations, respectively. $\varsigma_{\theta\phi} = \varsigma_{\phi\theta}$ is the covariance of θ and ϕ.

B. Cosinusoidal Ripple Model

The shape of the small-scale ripples depends upon the angle of repose of the inherent material. The ripples are periodic in the wind direction and are skewed, resulting in two distinct sides. The downwind side is steeper than the windward side. The spectrum of sand surface ripples are narrowband. Thus, ripples are modeled as a cosinusoidal wave. The wavelength of the cosinusoid corresponds to the dominant wavelength of the ripple spectrum. The near-surface wind direction changes rapidly over the undulating sand dune surface, inducing local variabilities in the ripple direction. In this paper, we treat ripples as not having any directional variability.

The scattering from periodic surfaces results in enhanced response at discrete directions called Floquet modes. The derivation of the scattering amplitudes and directions of the modes is presented in [20] and is applied in the model proposed here. The resulting Bragg scattering coefficient (σ_B) is a function of the surface orientation, surface ripple characteristics, incident wave characteristics, and the Floquet mode considered. It can be written as $\sigma_B(\hat{\mathbf{n}}, \overline{\mathbf{K}}, h, \overline{\mathbf{k}}, \hat{\mathbf{e}}, m)$ where h is the surface wave amplitude, and m is the Floquet mode. $\hat{\mathbf{e}}$ denotes the polarization of the incident wave. σ_B is computed using incident and backscattered power, which are given in [20, eqs. 3.2.61 and 3.2.62].

The scattering from the sand surface ripples is modeled using Bragg scattering theory. The derivation of Bragg backscattering look directions for a given surface tilt and cosinusoidal ripple is given in the Appendix. For a surface geometry given by $\hat{\mathbf{n}}$ and $\overline{\mathbf{K}}$, the incident wave vector $\overline{\mathbf{k}}$ that results in Bragg backscattering obeys conditions given by

$$(\widehat{\mathbf{K}} \times \hat{\mathbf{n}}) \cdot \hat{\mathbf{k}} = 0 \quad \widehat{\mathbf{K}} \cdot \hat{\mathbf{k}} = -\frac{mK}{2k}. \tag{9}$$

The first condition means that $\hat{\mathbf{k}}$ lies in the plane formed by $\hat{\mathbf{n}}$ and $\widehat{\mathbf{K}}$, i.e., the incident wave is directed along the direction of periodicity. The second condition is equivalent to $\sin\theta' = mK/2k$ specifying the Bragg incidence angles on a flat surface.

The solution of these two equations is given by

$$\hat{\mathbf{k}}_m = \pm\sqrt{1 - \left(\frac{mK}{2k}\right)^2}\,\hat{\mathbf{n}} - \frac{mK}{2k}\widehat{\mathbf{K}} \tag{10}$$

where $\hat{\mathbf{k}}_m$ is the incident wave vector that results in backscatter of the mth Floquet mode. The backscatter response from a cosinusoidal surface ripple is

$$\sigma^{\circ}_{\text{wave}}(\theta, \phi) = \sum_m \sigma_B(\hat{\mathbf{n}}, \overline{\mathbf{K}}, h, \overline{\mathbf{k}}, \hat{\mathbf{e}}, m)\delta(\hat{\mathbf{k}} - \hat{\mathbf{k}}_m) \tag{11}$$

where the delta function in the model assures that only modes in the backscatter direction contribute. Zero-mode Bragg backscattering direction ($\hat{\mathbf{k}}_0$) occurs when $\hat{\mathbf{k}} = \hat{\mathbf{n}}$. Bragg backscattering from surface ripples occurs only at discrete points in the θ—ϕ space, which are symmetric about the zero-mode direction. The Bragg backscatter directions closer to the zero-mode direction have a relatively higher backscattering return that decreases at higher local incidence angles. Fig. 6 shows the backscattering response from cosinusoidal ripples over a tilted facet. The zero-mode corresponds to $\theta = \theta_s = 15^\circ$ and $\phi = \phi_s = 180^\circ$. The high-magnitude Bragg backscattering directions occur close to the zero-mode point, as shown in Fig. 6. Thus, NSCAT and ESCAT σ° at incidence angles higher than 15° have a higher contribution from the ripples on tilted facets.

The sand ripples are periodic and band limited; hence, the total backscatter for N surface cosinusoids is

$$\sigma^{\circ}_{\text{ripples}}(\theta, \phi) = \sum_{n=1}^{N} \sum_m \sigma_B(\hat{\mathbf{n}}, \overline{\mathbf{K}}_n, h_n, \overline{\mathbf{k}}, \hat{\mathbf{e}}, m)\delta(\hat{\mathbf{k}} - \hat{\mathbf{k}}_m) \tag{12}$$

where $\overline{\mathbf{K}}_n$ and h_n are the nth surface cosinusoidal ripple's wave vector and amplitude, respectively.

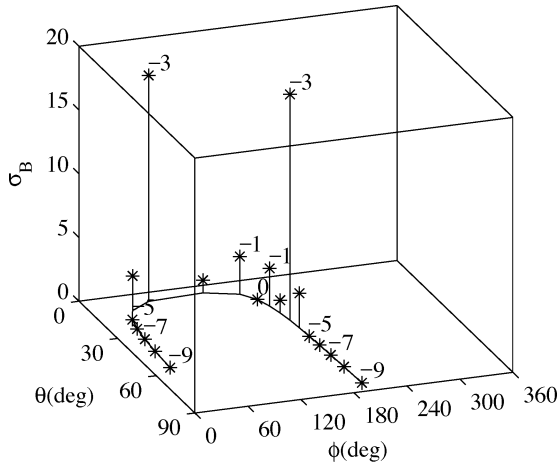

Fig. 6. Bragg backscattering response from cosinusoidal surface ripples of wavelength 10 cm and amplitude 1.5 cm in $\phi_K = 20^\circ$ direction over a facet with (15°, 180°) tilt as a function of the observation angles θ and ϕ. The negative numbers next to data points are the Floquet modes backscattered at that direction.

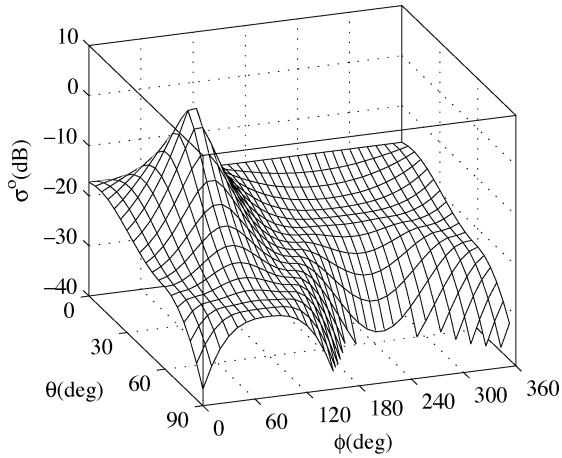

Fig. 7. Model σ° response [(4)] from a single rough surface facet with $\theta_n = 30^\circ$, $\phi_n = 75^\circ$ and Gaussian tilt distribution having $\varsigma_\theta = \varsigma_\phi = 1$, $\varsigma_{\theta\phi} = 0$ with $\sigma_s = -21.09 - 0.301(\theta - 40^\circ) + 0.0092(\theta - 40^\circ)^2$.

IV. Rough Facet Model Simulation

In this section, we present model simulations over simple dunes, i.e., transverse and longitudinal dunes. First, we illustrate the result for a single rough facet. Fig. 7 shows the modeled backscatter response from a single rough surface facet with a Gaussian tilt distribution with $\theta_n = 30^\circ, \phi_n = 75^\circ, \varsigma_\theta = \varsigma_\phi = 1$, and $\varsigma_{\theta\phi} = 0$. Although covariance between θ_s and ϕ_s is related through the wind characteristics and the grain distribution, in the present analysis we assume θ_s and ϕ_s are uncorrelated in order to keep the simulation simple. The $\sigma_s(\theta)$ used is the quadratic fit and extension from Fig. 5. The simulated $\sigma^\circ(\theta, \phi)$ response peaks when $\theta = \theta_n$ and $\phi = \phi_n$ and thus clearly reflects the facet characteristics. The standard deviations of the tilt angles affect the height of the peak and gradient in its vicinity. The parabolic bite at high incidence angles corresponds to directions beyond the grazing angle of the facet and hence do not result in any backscattering.

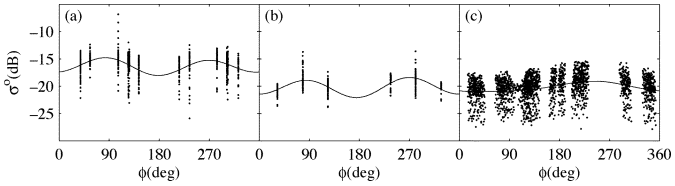

Fig. 8. σ° azimuth angle response over a longitudinal dune field at (17.5°N, 15.35°W) from (a) NSCAT V-pol for θ in the range 30° to 35°, (b) ESCAT for θ in the range 30° to 35°, and (c) QSCAT for $\theta = 55°$. Solid line is a second-order harmonic fit.

When modeled as composed of rough surface facets, the $\sigma^\circ(\theta, \phi)$ response of dunes is the linear combination of the individual rough facet responses. Sections IV-A and IV-B describe the rough surface facet models for transverse and longitudinal dunes and their $\sigma^\circ(\theta, \phi)$ response when applied to the model. The results are compared to the observations made by NSCAT and ESCAT over areas of known dune types.

A. Longitudinal Dune

A longitudinal dune has two opposite slip-sides. The slip-sides have a slope equal to the angle of repose of the parent sand, which is nominally taken to be 30° to 35° and corresponds to a mean tilt angle of θ_n. The azimuth orientation of the two slip-sides are, in general, separated by 180°.

In order to model the longitudinal dune field, we analyze the $\sigma^\circ(\theta)$ and $\sigma^\circ(\phi)$ responses observed by NSCAT, ESCAT, and QSCAT. Fig. 8 illustrates the azimuth angle modulation of σ° observations at location 11 (17.5°N, 15.35°W). NSCAT and ESCAT give similar results in which the two maxima correspond to the orientation of the two slip-sides of the longitudinal dune. The two maxima are separated by approximately 180° in azimuth. The NSCAT and ESCAT incidence angles in Fig. 8 result in normal local incidence angle observation of the slip-sides at the azimuth angles of the graph maxima. Since these slip-sides are a result of an average wind direction parallel to the axis of the dune, the wind direction producing this dune lies between the two peaks with an ambiguity of 180°. The ESCAT σ° is lower than NSCAT due to its longer wavelength, resulting in greater penetration and thus higher loss. QSCAT has reduced ϕ modulation because of its high incidence angle, which does not result in normal incidence angle observation of the slip-sides.

The effect of slip-sides in the observed σ° is further confirmed by analysing the $\sigma^\circ(\theta)$ response at the azimuth angles corresponding to the maxima in azimuth modulation. Fig. 9 presents such plots for both ESCAT and NSCAT measurements. The data are fit with a nonparametric line curve. A rise in the σ° measurements in the 30° to 35° incidence angle range is observed, particularly in Fig. 9(a) and (c).

The analysis of $\sigma^\circ(\theta)$ and $\sigma^\circ(\phi)$ responses from the observed data confirms that the σ° behavior can be explained by considering the sides of the longitudinal dune as rough facets. We model the longitudinal dune field as two tilted rough facets and a flat rough facet between parallel dunes. Fig. 10 shows the correspondence between a typical longitudinal dune and the rough facet model. The two rough facets have mean tilts $(32° \pm 2°, \phi_n)$ and $(32° \pm 2°, \phi_n + 180°)$, and the third rough facet with

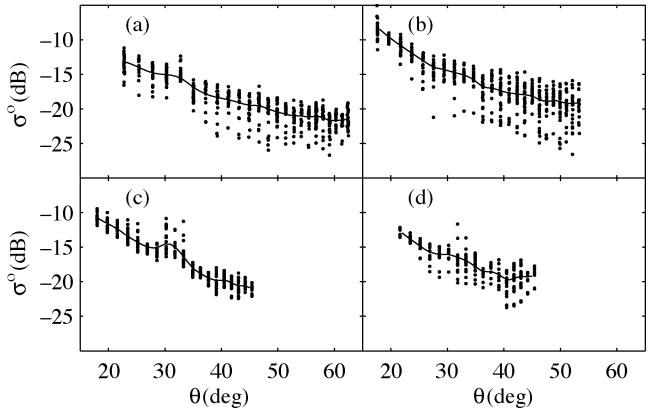

Fig. 9. σ° incidence angle response over a longitudinal dune field at (17.5°N, 15.35°W) from NSCAT V-pol and ESCAT. (a) and (b) are NSCAT measurements at $\phi = 56°$ and $\phi = 284°$, respectively. (c) and (d) are ESCAT measurements at $\phi = 79°$ and at $\phi = 218°$, respectively.

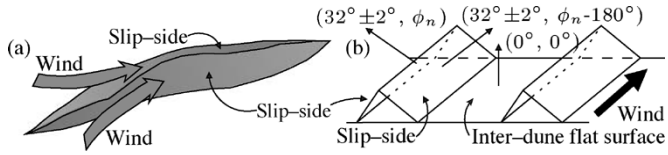

Fig. 10. (a) Longitudinal dune and (b) its facet model.

mean tilt (0°, 0°) (flat) is used to represent the interdune space in a longitudinal dune field. All of these facets are modeled with a Gaussian tilt distribution. The fraction of the footprint covered by each slip-side (F_s) is the same due to the symmetry of the longitudinal dunes, and hence, the flat rough facet covers a $F_f = 1 - 2F_s$ fraction of the footprint.

In order to apply (5) as a forward model, we interchange the order of integrations and summation to obtain

$$\sigma^\circ_{\text{dunes}}(\theta, \phi) = \int_0^{2\pi} \int_0^{\frac{\pi}{2}} P_T(\theta_s, \phi_s) \sigma_s(\theta', \phi') u(\theta_g - \theta) d\theta_s d\phi_s \tag{13}$$

where $P_T(\theta_s, \phi_s) = \sum_n F_n P_n(\theta_s, \phi_s)$ is the weighted total of the tilt distributions of the dominant facets in the footprint. Fig. 11(a) shows the cumulative tilt distribution for the modeled longitudinal dune field. The two peaks at (30°, 60°) and (30°, 240°) are due to two slip-sides with equal weights of 25% and the third long peak corresponds to the flat rough facet (0°, 0°) with a 50% weight. The σ° response for this tilt distribution is shown in Fig. 11(b) where $\sigma_s(\theta)$ is computed from NSCAT and TRMM data at location 11, similar to Fig. 5. The presence of three dominant facets shows up in the modeled σ° response in the form of peaks. This result is consistent to the observations made by NSCAT [Fig. 11(c)] and ESCAT [Fig. 11(d)] over the areas of longitudinal dune fields in the Sahara. The mesh of NSCAT and ESCAT $\sigma^\circ(\theta, \phi)$ response is prepared by using the σ° versus θ observations at each ϕ sample and fitting the data with a nonparametric curve similar to Fig. 9. The line fits for different ϕ directions are then connected at regular θ intervals to achieve the mesh plots in Fig. 11(c) and (d) for comparison with model simulation. The peaks at (32°, 106.5°) and (32°, 302.5°) in NSCAT data and at (31°, 79°) and (31°, 281°) in ESCAT data

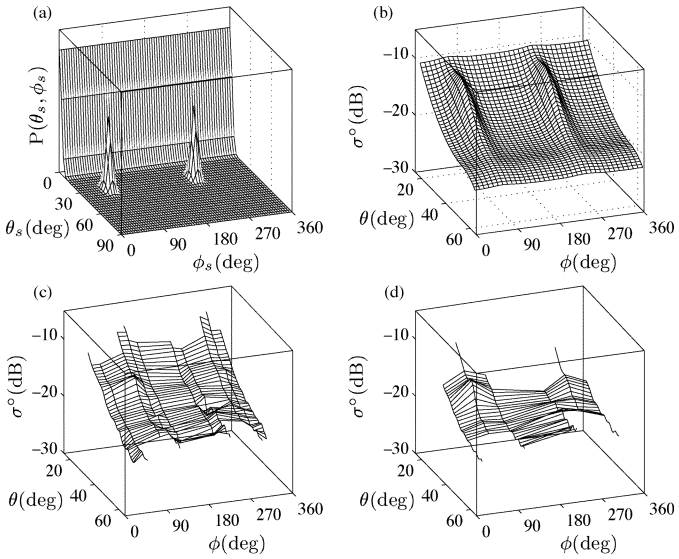

Fig. 11. (a) Tilt distribution of a longitudinal dune with each slip-side covering 25% of footprint. The orientation of the slip-sides is (30°, 60°) and (30°, 240°) with $\varsigma_\theta = 3°$, $\varsigma_\phi = 5°$ and $\varsigma_{\theta\phi} = 0$. Interdune flat area covers the remaining 50% of surface with $\varsigma_\theta = 3°$, $\varsigma_\phi = 6°$, and $\varsigma_{\theta\phi} = 0$. (b) Corresponding simulated σ° response using $\sigma_s = -18.82 - 0.24(\theta - 40°) + 0.0088(\theta - 40°)^2$. Observation over actual longitudinal dune field at (17.5°N, 15.35°W) by (c) NSCAT V-pol and (d) ESCAT.

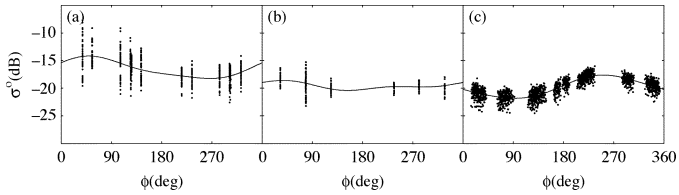

Fig. 12. σ° azimuth angle response over a transverse dune field at (17.5°N, 9.3°W) from (a) NSCAT V-pol for θ range 30° to 35°, (b) ESCAT for θ range 30° to 35°, and (c) QSCAT for $\theta = 55°$. Solid line is a second-order harmonic fit.

are the responses due to the two slip-sides of the longitudinal dunes in the footprint. Since the slip-sides have slopes nearly equal to the angle of repose, they are almost devoid of any surface ripples.

B. Transverse Dune

A typical transverse dune has two sides, a slip-side similar to longitudinal dunes and a windward-side, which is opposite to the slip-side in azimuth and has a slope of 10° to 15°. Fig. 12 shows $\sigma^\circ(\phi)$ plots for NSCAT, ESCAT, and QSCAT over a transverse dune field at (17.5°N, 9.3°W). The single maximum corresponds to the single slip-side of a transverse dune. In this case, the azimuth angle corresponding to this maximum is the mean wind direction that produces this dune field.

Fig. 13 shows $\sigma^\circ(\theta)$ modulation over the slip- and windward-side of a transverse dune from NSCAT and ESCAT observations. The slip-side response has a rise in σ° in the incidence angle range of 30° to 35° similar to the longitudinal slip-side. This observation is consistent in both Ku- and C-band data. Since the slope of the windward-side is lower than the slip-side, it results in a similar σ° rise at incidence angles of 10° to 15° (not observed by scatterometers).

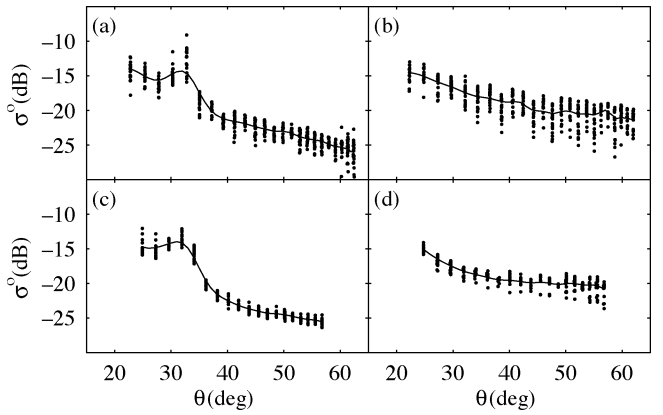

Fig. 13. σ° incidence angle response over a transverse dune field at (17.5°N, 9.3°W) from NSCAT V-pol and ESCAT. (a) and (b) are NSCAT measurements at $\phi = 56°$ and $\phi = 284°$, respectively. (c) and (d) are ESCAT measurements at $\phi = 33°$ and at $\phi = 236°$, respectively.

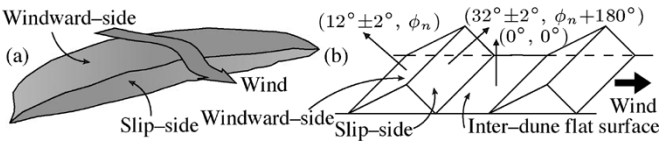

Fig. 14. (a) Transverse dune and (b) its facet model.

The $\sigma^\circ(\theta)$ and $\sigma^\circ(\phi)$ responses of the observations show that the sides of a transverse dune can be viewed as facets. We model the slip- and windward-sides of transverse dunes as rough surface facets with (30° to 35°, ϕ_n) and (10° to 15°, $\phi_n + 180°$) mean tilt, respectively. The dune fields are modeled as composed of many simple dunes with interdune areas modeled as zero tilt rough facets similar to longitudinal dune fields. The model is shown in Fig. 14.

The geometry of the transverse dunes suggests that the ratio of windward- and slip-side area (F_w/F_s) is in the range 2.2–2.8 and that the flat area fraction is $F_f = 1 - F_w - F_s$. Fig. 15(a) shows the cumulative tilt distribution for the modeled transverse dune field. The two peaks at (30°, 60°) and (12°, 240°) are due to slip- and windward-side with weights of 15% and 35%, respectively. The third long peak corresponds to the flat rough facet (0°, 0°) with 50% weight. The σ° response for this tilt distribution is shown in Fig. 15(b) where $\sigma_s(\theta)$ is computed from NSCAT and TRMM data at location 8, similar to Fig. 5. The presence of three dominant facets shows up in the modeled σ° response in the form of peaks. This result is consistent with observations made by NSCAT [Fig. 15(c)] and ESCAT [Fig. 15(d)] over areas of transverse dune fields in the Sahara. The observations are similar to longitudinal dunes but have only one slip-side response. However, unlike longitudinal dunes, there is a peak 180° in azimuth from the slip-side at higher incidence angles. This peak is due to Bragg Scattering from the small-scale ripples on the windward-side of the transverse dune.

The model simulation results for both longitudinal and transverse dune fields significantly resemble the scatterometer observations. This is further confirmed by the consistent response from the two scatterometers operating at different frequencies. The results can be extended to more complicated dunes where

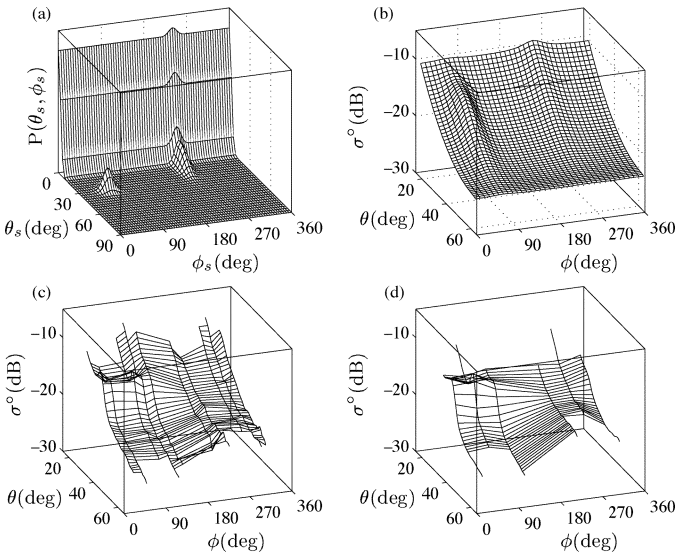

Fig. 15. (a) Tilt distribution of a transverse dune with slip- and windward-side covering 15% and 35% of footprint, respectively. Slip-side is oriented in (30°, 60°) direction with $\varsigma_\theta = 3°$, $\varsigma_\phi = 10°$, and $\varsigma_{\theta\phi} = 0$. Windward-side is oriented in (30°, 240°) direction with $\varsigma_\theta = 8°$, $\varsigma_\phi = 8°$, and $\varsigma_{\theta\phi} = 0$. Interdune flat area covers the remaining 50% of surface with $\varsigma_\theta = 3°$, $\varsigma_\phi = 8°$, and $\varsigma_{\theta\phi} = 0$. (b) Corresponding simulated σ° response using $\sigma_s = -20.05 - 0.328(\theta - 40°) + 0.0075(\theta - 40°)^2$. Observation over actual transverse dune field at (17.5°N, 9.3°W) by (c) NSCAT V-pol and (d) ESCAT.

the number of facets increases and facet orientation is more variable. Crescent-shaped barchan's facets have the same tilts as transverse dunes but with higher ϕ_s variance. The high variance reflects the directional variability of the tilted facets in the form of the curvature of Barchan slip- and windward-side.

Star dunes, due to multiple limbs extending in various directions, result in increased σ° variability with the look direction. Sand sheets without dunes show negligible azimuth angle modulation and have linear incidence angle response (in decibel scale). Observations show that the incidence angle response becomes more quadratic with increasing thickness of the sand layer.

C. Summary

The electromagnetic scattering from erg surfaces is modeled as composed of scattering from large-scale dunes and small-scale ripples. The dunes are modeled as composed of tilted rough facets. The total scattering due to dunes is the sum of scattering from all of the rough facets in the footprint weighted by the fraction of their area in the footprint. Small-scale ripples are modeled as cosinusoidal ripples that scatter the incident electromagnetic waves in discrete directions called Floquet modes. The backscattering from the cosinusoidal ripples occurs in the directions that have Floquet modes directed toward the sensor. The total backscattering response of surface ripples is the sum of scattering from all of the surface components.

We model longitudinal and transverse dune fields as composed of three dominant rough facets. Two of these facets correspond to the two slip-sides in the case of longitudinal dunes. For transverse dunes, they correspond to windward- and slip-side. The third facet is flat and accounts for the interdune flat area. The proposed rough facet model is applied to the modeled dune fields. The results indicate a strong signature of the rough facets in the backscatter response. The look directions at which the peak value occurs give the mean tilt of the facet. The simulation results are similar to NSCAT and ESCAT observations over the Saharan longitudinal and transverse dune fields.

V. Conclusion

Ergs represent diverse and dynamic parts of the Sahara that undergo a continuous surface reformation due to wind action. Ergs have two scales of surface features. The large-scale features are dunes with dimensions ranging from meters to a few hundred meters. The small-scale features are surface periodic ripples with wavelengths from a few to tens of centimeters.

It is found that an erg surface modulates the Ku- and C-band σ° measurements with the look direction. The incidence angle modulation reflects the presence of slip-sides on the surface in the form of a slight rise in backscatter at the incidence angles equal to the angle of repose of sand. At these incidence angles, the azimuth modulation indicates the number of slip-sides present that can be used to identify the transverse and longitudinal dunes. This can be used to determine the average wind direction in the area.

Appendix

This appendix summarizes the derivation of geometric relations between the local incidence, azimuth, and grazing angles of a tilted rough facet. The view directions of a cosinusoidal wave on the rough facet that result in Bragg backscattering are also derived.

Consider a rough facet that has a unit surface normal vector $\hat{\mathbf{n}}$ and cosinusoidal surface wave with period λ_s represented by $\overline{\mathbf{K}} = K\hat{\mathbf{K}}$ where $K = 2\pi/\lambda_s$ (see Fig. 4). Let the electromagnetic wave with a wave vector $\overline{\mathbf{k}} = k\hat{\mathbf{k}}$ be incident on the surface. Here, $k = 2\pi/\lambda$ with λ being the wavelength of the incident wave. Fig. 4 also depicts spherical angles of these vectors relative to the principal coordinate system ($\hat{\mathbf{x}}$, $\hat{\mathbf{y}}$, $\hat{\mathbf{z}}$).

A. Local Incidence and Azimuth Angles

The local normal vector $\hat{\mathbf{n}}$ and incidence wave vector $\hat{\mathbf{k}}$ are

$$\hat{\mathbf{n}} = \sin\theta_s\cos\phi_s\hat{\mathbf{x}} + \sin\theta_s\sin\phi_s\hat{\mathbf{y}} + \cos\theta_s\hat{\mathbf{z}} \quad (14)$$

$$\hat{\mathbf{k}} = \sin\theta\cos\phi\hat{\mathbf{x}} + \sin\theta\sin\phi\hat{\mathbf{y}} + \cos\theta\hat{\mathbf{z}}. \quad (15)$$

The slopes of the surface in x and y directions are given by

$$Z_x = -\frac{\sin\theta_s}{\cos\theta_s}\cos\phi_s \quad (16)$$

$$Z_y = -\frac{\sin\theta_s}{\cos\theta_s}\sin\phi_s \quad (17)$$

where the inverse relationship is given by

$$\theta_s = \tan^{-1}\left(\sqrt{Z_x^2 + Z_y^2}\right) \quad (18)$$

$$\phi_s = \tan^{-1}\left(\frac{Z_y}{Z_x}\right). \quad (19)$$

We define the local coordinate system ($\hat{\mathbf{x}}'$, $\hat{\mathbf{y}}'$, $\hat{\mathbf{z}}'$) as

$$\hat{\mathbf{z}}' = \hat{\mathbf{k}} \quad (20)$$

$$\hat{\mathbf{x}}' = \cos\theta\cos\phi\hat{\mathbf{x}} + \cos\theta\sin\phi\hat{\mathbf{y}} - \sin\theta\hat{\mathbf{z}} \quad (21)$$

$$\hat{\mathbf{y}}' = \hat{\mathbf{z}}' \times \hat{\mathbf{x}}' = -\sin\phi\hat{\mathbf{x}} + \cos\phi\hat{\mathbf{y}}. \quad (22)$$

In the $(\hat{\mathbf{x}}', \hat{\mathbf{y}}', \hat{\mathbf{z}}')$ coordinates $\hat{\mathbf{n}}$ is

$$\hat{\mathbf{n}}' = (\hat{\mathbf{n}} \cdot \hat{\mathbf{x}}')\hat{\mathbf{x}}' + (\hat{\mathbf{n}} \cdot \hat{\mathbf{y}}')\hat{\mathbf{y}}' + (\hat{\mathbf{n}} \cdot \hat{\mathbf{z}}')\hat{\mathbf{z}}'. \tag{23}$$

The surface slope expressed in the local coordinate system is

$$Z'_x = -\frac{\hat{\mathbf{n}} \cdot \hat{\mathbf{x}}'}{\hat{\mathbf{n}} \cdot \hat{\mathbf{z}}'} \tag{24}$$

$$Z'_y = -\frac{\hat{\mathbf{n}} \cdot \hat{\mathbf{y}}'}{\hat{\mathbf{n}} \cdot \hat{\mathbf{z}}'}. \tag{25}$$

Hence, the spherical angles of $\hat{\mathbf{n}}$ in the local coordinates are given as

$$\theta' = \tan^{-1}\left(\frac{\sqrt{(\hat{\mathbf{n}} \cdot \hat{\mathbf{x}}')^2 + (\hat{\mathbf{n}} \cdot \hat{\mathbf{y}}')^2}}{\hat{\mathbf{n}} \cdot \hat{\mathbf{z}}\prime}\right) \tag{26}$$

$$\phi' = \tan^{-1}\left(\frac{\hat{\mathbf{n}} \cdot \hat{\mathbf{y}}'}{\hat{\mathbf{n}} \cdot \hat{\mathbf{x}}'}\right). \tag{27}$$

B. Grazing Angle

The local grazing angle θ_g is elevation angle of $\hat{\mathbf{k}}_g$ in the global coordinates, where $\hat{\mathbf{k}}_g$ is a unit vector in the direction of the projection of $\overline{\mathbf{k}}$ on the facet, is given by

$$\hat{\mathbf{k}}_g = \frac{\hat{\mathbf{n}} \times (\hat{\mathbf{k}} \times \hat{\mathbf{z}})}{\left|\hat{\mathbf{n}} \times (\hat{\mathbf{k}} \times \hat{\mathbf{z}})\right|} = \frac{(\hat{\mathbf{z}} \cdot \hat{\mathbf{n}})\hat{\mathbf{k}} - (\hat{\mathbf{n}} \cdot \hat{\mathbf{k}})\hat{\mathbf{z}}}{\left|\hat{\mathbf{n}} \times (\hat{\mathbf{k}} \times \hat{\mathbf{z}})\right|} \tag{28}$$

$$\tan\theta_g = \frac{|\hat{\mathbf{k}}_g \times \hat{\mathbf{z}}|}{\hat{\mathbf{k}}_g \cdot \hat{\mathbf{z}}} \tag{29}$$

$$= \frac{(\hat{\mathbf{n}} \cdot \hat{\mathbf{z}})\sqrt{1 - (\hat{\mathbf{k}} \cdot \hat{\mathbf{z}})^2}}{(\hat{\mathbf{n}} \cdot \hat{\mathbf{z}})(\hat{\mathbf{k}} \cdot \hat{\mathbf{z}}) - (\hat{\mathbf{n}} \cdot \hat{\mathbf{k}})} \tag{30}$$

$$= -\frac{1}{\tan\theta_s \cos(\phi_s - \phi)}. \tag{31}$$

C. Bragg Look Directions

A periodic surface causes the incident wave to be scattered in discrete directions called Floquet modes [20]. For Bragg backscattering to occur, there must be a Floquet mode in the direction of the sensor. This condition can be written in vector form as

$$(\widehat{\mathbf{K}} \times \hat{\mathbf{n}}) \cdot \hat{\mathbf{k}} = 0 \quad \text{(i.e., vectors must be coplanar)} \tag{32}$$

$$\widehat{\mathbf{K}} \cdot \hat{\mathbf{k}} = -\frac{mK}{2k}. \tag{33}$$

For a rippled rough surface facet geometry specified by $\hat{\mathbf{n}}$ and $\widehat{\mathbf{K}}$, we can find all look directions $\hat{\mathbf{k}}_m$ that result in Bragg backscattering. Here, m represents the Floquet mode that is backscattered. Multiplying (32) and (33) by $\widehat{\mathbf{K}}$ and $(\widehat{\mathbf{K}} \times \hat{\mathbf{n}})$, respectively, and then subtracting the two we obtain

$$\widehat{\mathbf{K}}\left\{(\widehat{\mathbf{K}} \times \hat{\mathbf{n}}) \cdot \hat{\mathbf{k}}_m\right\} - (\widehat{\mathbf{K}} \times \hat{\mathbf{n}})(\widehat{\mathbf{K}} \cdot \hat{\mathbf{k}}_m) = \frac{mK}{2k}(\widehat{\mathbf{K}} \times \hat{\mathbf{n}}) \tag{34}$$

$$\text{since } \widehat{\mathbf{K}} \cdot \hat{\mathbf{n}} = 0 \quad -\hat{\mathbf{k}}_m \times \hat{\mathbf{n}} = \frac{mK}{2k}(\widehat{\mathbf{K}} \times \hat{\mathbf{n}}) \tag{35}$$

$$\left(\hat{\mathbf{k}}_m + \frac{mK}{2k}\widehat{\mathbf{K}}\right) \times \hat{\mathbf{n}} = \mathbf{0}. \tag{36}$$

The null cross product indicates that the two vectors are colinear, and hence, one can be written as a scalar multiple of the other as $\hat{\mathbf{k}}_m + (mK/2k)\widehat{\mathbf{K}} = t\hat{\mathbf{n}}$ and the Bragg backscattering direction as $\hat{\mathbf{k}}_m = t\hat{\mathbf{n}} - (mK/2k)\widehat{\mathbf{K}}$, where t is some scalar. t can be found using the fact that $\hat{\mathbf{k}}_m \cdot \hat{\mathbf{k}}_m = 1$; hence

$$\left\{t\hat{\mathbf{n}} - \frac{mK}{2k}\widehat{\mathbf{K}}\right\} \cdot \left\{t\hat{\mathbf{n}} - \frac{mK}{2k}\widehat{\mathbf{K}}\right\} = t^2 + \left(\frac{mK}{2k}\right)^2 = 1. \tag{37}$$

Thus, the Bragg backscattering directions can be written as

$$\hat{\mathbf{k}}_m = \pm\sqrt{1 - \left(\frac{mK}{2k}\right)^2}\,\hat{\mathbf{n}} - \frac{mK}{2k}\widehat{\mathbf{K}}. \tag{38}$$

REFERENCES

[1] R. U. Cooke and A. Warren, *Geomorphology of Deserts*. London, U.K.: Anchor Press, 1973.

[2] A. S. Goudie, I. Livingstone, and S. Stokes, *Aeolian Environments, Sediments and Landforms*. London, U.K.: Wiley, 1999.

[3] R. G. Kennett and F. K. Li, "Seasat over-land scatterometer data, part I: Global overview of the Ku-band backscatter coefficients," *IEEE Trans. Geosci. Remote Sens.*, vol. 27, no. 5, pp. 592–605, Sep. 1989.

[4] K. Pye and H. Tsoar, *Aeolian Sand and Sand Dunes*. London, U.K.: Unwin Hyman, 1990.

[5] R. A. Bagnold, *The Physics of Blown Sand and Desert Dunes*. London, U.K.: Methuen, 1941.

[6] F. M. Naderi, M. H. Freilich, and D. G. Long, "Spaceborne radar measurement of wind velocity over the ocean—An overview of the NSCAT scatterometer system," *Proc. IEEE*, vol. 79, no. 6, pp. 850–866, Jun. 1992.

[7] Q. P. Remund, D. G. Long, and M. R. Drinkwater, "An iterative approach to multisensor sea ice classification," *IEEE Trans. Geosci. Remote Sens.*, vol. 38, no. 4, pp. 1843–1856, Jul. 2000.

[8] D. G. Long and P. J. Hardin, "Vegetation studies of the Amazon basin using enhanced resolution Seasat scatterometer data," *IEEE Trans. Geosci. Remote Sens.*, vol. 32, no. 2, pp. 449–460, Mar. 1994.

[9] D. G. Long and M. R. Drinkwater, "Cryosphere applications of NSCAT data," *IEEE Trans. Geosci. Remote Sens.*, vol. 37, no. 3, pp. 1671–1684, May 1999.

[10] M. Spencer, C. Wu, and D. G. Long, "Tradeoffs in the design of a spaceborne scanning pencil beam scatterometer: Application to SeaWinds," *IEEE Trans. Geosci. Remote Sens.*, vol. 35, no. 1, pp. 115–126, Jan. 1997.

[11] T. Kozu, T. Kawanishi, H. Kuroiwa, M. Kojima, K. Oikawa, H. Kumagai, K. Okamoto, M. Okumura, H. Nakatsuka, and K. Nishikawa, "Development of precipitation radar onboard the Tropical Rainfall Measuring Mission (TRMM) satellite," *IEEE Trans. Geosci. Remote Sens.*, vol. 39, no. 1, pp. 102–116, Jan. 2001.

[12] E. P. W. Attema, "The active microwave instrument on-board the ERS-1 satellite," *Proc. IEEE*, vol. 79, no. 6, pp. 791–799, Jun. 1991.

[13] E. D. McKee, *A Study of Global Sand Seas: Geological Survey Professional Paper 1052*. Washington, DC: U.S. Gov. Printing Office, 1979.

[14] C. T. Swift, "Seasat scatterometer observations of sea ice," *IEEE Trans. Geosci. Remote Sens.*, vol. 37, no. 2, pp. 716–723, Mar. 1999.

[15] W. J. Plant, "A two-scale model of short wind-generated waves and scatterometery," *J. Geophys. Res.*, vol. 91, no. C9, pp. 10 735–10 749, 1986.

[16] A. I. Kozlov, L. P. Ligthart, and A. I. Logvin, *Mathematical and Physical Modeling of Microwave Scattering and Polarimetric Remote Sensing*. Dordrecht, The Netherlands: Kluwer, 2001.

[17] F. Ulaby, R. Moore, and A. Fung, *Microwave Remote Sensing: Active and Passive*. Norwood, MA: Artech House, 1982, vol. 2.

[18] H. L. Chan and A. K. Fung, "A theory of sea scatter at large incident angles," *J. Geophys. Res.*, vol. 82, no. 24, pp. 3439–3444, 1977.

[19] D. R. Lyzenga and J. F. Vesecky, "Two-scale polarimetric emissivity model: Efficiency improvements and comparisons with data," *Progr. Electromagn.*, vol. PIER-37, pp. 205–219, 2002.

[20] J. A. Kong, *Electromagnetic Wave Theory*. Cambridge, MA: EMW, 1999.

Haroon Stephen (S'97) received the M.S. degree in remote sensing and geographic information systems from the Asian Institute of Technology (AIT), Bangkok, Thailand, in 1997. He is currently pursuing the Ph.D. degree in electrical engineering at Brigham Young University (BYU), Provo, UT.

From 1997 to 1998, he was with the European Space Agency office at AIT, where he investigated scatterometer applications for land surfaces. During this time he also taught short courses in remote sensing. He joined the Microwave Earth Remote Sensing Research Group at BYU in 1999. His current research interests are remote sensing of sand surfaces and tropical vegetation using spaceborne scatterometers and radiometers.

David G. Long (S'80–SM'98) received the Ph.D. degree in electrical engineering from the University of Southern California, Los Angeles, in 1989.

From 1983 to 1990, he was with the National Aeronautics and Space Administration (NASA) Jet Propulsion Laboratory (JPL), Pasadena, CA, where he developed advanced radar remote sensing systems. While at JPL, he was the Senior Project Engineer on the NASA Scatterometer (NSCAT) project, which was flown aboard the Japanese Advanced Earth Observing System (ADEOS) from 1996 to 1997. He was also the Experiment Manager and Project Engineer for the SCANSCAT scatterometer (now known as SeaWinds). In 1990, he joined the Department of Electrical and Computer Engineering, Brigham Young University (BYU), Provo, UT, where he currently teaches upper division and graduate courses in communications, microwave remote sensing, radar, and signal processing, is the Director of BYU's Center for Remote Sensing, and is the Head of the Microwave Earth Remote Sensing Laboratory. He is the Principal Investigator on several NASA-sponsored interdisciplinary research projects in microwave remote sensing and innovative radar systems. He has numerous publications in signal processing and radar scatterometry. His research interests include microwave remote sensing, radar, polar ice, signal processing, estimation theory, and mesoscale atmospheric dynamics. He has over 250 publications in the open literature.

Dr. Long has received the NASA Certificate of Recognition several times. He is an Associate Editor for the IEEE GEOSCIENCE AND REMOTE SENSING LETTERS.